Imaging and control of critical fluctuations in two-dimensional magnets

Chenhao Jin[1*], Zui Tao[1,2], Kaifei Kang[2], Kenji Watanabe[3], Takashi Taniguchi[3], Kin Fai Mak[1,2,4*], Jie Shan[1,2,4*]

[1] Kavli Institute at Cornell for Nanoscale Science, Ithaca, NY 14853, USA

[2] School of Applied and Engineering Physics, Cornell University, Ithaca, NY 14853, USA

[3] National Institute for Materials Science, 1-1 Namiki, Tsukuba, 305-0044, Japan.

[4] Laboratory of Atomic and Solid State Physics, Cornell University, Ithaca, NY 14853, USA.

* Correspondence to: jinchenhao@cornell.edu, km627@cornell.edu, jie.shan@cornell.edu

Abstract:

Strong magnetization fluctuations are expected near the thermodynamic critical point of a continuous magnetic phase transition. Such critical fluctuations are highly correlated and in principle can occur at any time- and length-scales[1]; they govern critical phenomena and potentially can drive new phases[2,3]. Although critical phenomena in magnetic materials have been studied using neutron scattering, magnetic AC susceptibility and other techniques [4-6], direct real-time imaging of critical magnetization fluctuations remains elusive. Here we develop a fast and sensitive magneto-optical imaging microscope to achieve wide-field, real-time monitoring of critical magnetization fluctuations in single-layer ferromagnetic insulator $CrBr_3$. We track the critical phenomena directly from the fluctuation correlations and observe both slowing-down dynamics and enhanced correlation length. Through real-time feedback control of the critical fluctuations, we further achieve switching of magnetic states solely by electrostatic gating. The ability to directly image and control critical fluctuations in 2D magnets opens up exciting opportunities to explore critical phenomena and develop applications in nanoscale engines and information science.

Two-dimensional (2D) van der Waals magnets have attracted much recent interest[2,3,7-19]. As atomically-thin layers, they have been incorporated into van der Waals heterostructures and device architectures to enable novel functionalities, such as gate-controllable magnetism and spin-filter tunneling[9-14]. The 2D nature of layered magnets also leads to distinct physical properties from that of their bulk counterparts, ranging from stacking-dependent magnetism to topological spin excitations[15-19]. Of particular interest are magnetization fluctuations near a thermodynamic critical point[2,3], which are crucial to understanding magnetism in two dimensions but remain largely unexplored experimentally. In three dimensions the phase space for thermal fluctuations to become critical is small and difficult to access according to the Ginzburg criterion[1,20]. In one-dimension fluctuations are so strong that magnetic long-range order is typically destroyed[21]. 2D layered magnets, in which fluctuations and long-range order reach a good balance, are therefore ideal to access and harness critical magnetization fluctuations.

Here we demonstrate real-time imaging of critical magnetization fluctuations and direct determination of their temporal and spatial correlations in single-layer ferromagnetic insulator $CrBr_3$ by a fast and sensitive magneto-optical imaging technique. We observe macroscopic spatial correlations and orders-of-magnitude change in the correlation time within around 0.5 K of the Curie temperature T_c. The observed extreme sensitivity of magnetization fluctuations to environment is different from non-critical thermal fluctuations in miniscule systems, and enables unprecedented flexibility for control. We are thereby able to switch the magnetic state of 2D $CrBr_3$ in a non-volatile, magnetic-field-free and current-free manner by harnessing critical fluctuations as a stochastic driving force, i.e. by toggling the critical fluctuations based on a real-time measurement of the magnetic state.

Being stochastic in nature, direct observation of critical fluctuations in real-time for a large sample area is challenging. We have developed a real-time magnetic circular dichroism (MCD) imaging technique that combines high temporal (up to 100 frames per second) and spatial (~ 600 nm) resolution with high sensitivity, which allows us to monitor the magnetization fluctuations in a single-layer ferromagnet $CrBr_3$. Figure 1a shows an illustration of our experimental setup. It enhances the optical contrast of MCD through polarization control (see Supplementary Note 2 and Methods). The concept of polarization control is well known in polarization microscopy, but the enhancement of the optical contrast is limited by the low polarization extinction ratio, which is typically several hundred due to polarization distortion from high numerical-aperture (NA) objectives[22,23]. The key improvement of our technique is to separate the effective NA for illumination and imaging: A long-focal-length lens L1 focuses the illumination beam roughly at the back aperture of an objective, minimizing the effective NA for illumination and thus polarization distortion. Similarly, specular-reflected light from a featureless substrate also maintains high polarization purity. However, scattered light from features on the sample is collected with the large effective NA of the objective. The spatial resolution is thus not compromised, as there is no physical aperture limiting the NA in the collection path. We are therefore able to achieve simultaneously a high extinction ratio ($> 3\times10^4$) and high spatial resolution (~ 600 nm) over the entire field of view. In this configuration, the optical contrast is approximately proportional to the MCD signal (and therefore also the out-of-plane magnetization of the sample), but is enhanced by more than 100 times compared to the MCD signal without polarization control. In addition, because the MCD signal is determined by the dielectric function of the sample and the local field factor of the environment, we can optimize the substrate to further improve the optical contrast by a few times (see Supplementary Note 3).

Figure 1b shows an optical microscopy image of a monolayer $CrBr_3$ sample S1 (inside the white dashed box), which is encapsulated with hexagonal boron nitride (hBN) on both sides. It shows a giant magneto-optical contrast of ±60% for the two remanent magnetization states at 18 K (Fig.1c and 1d), which are prepared by cooling the sample under an out-of-plane magnetic field of different polarities. Here the optical contrast is evaluated by using reflection from the $CrBr_3$ sample above T_c as reference. A nearby $CrBr_3$ flake (inside the green dashed box) can also be seen, but will not be focused on because of its smaller size. We first characterize the $CrBr_3$ monolayer (averaged over a 3x3 μm area in the center) away from T_c. The magnetization against magnetic field shows a hysteresis loop below T_c and paramagnetic behavior above T_c (Fig. 1e). We extract the remanent magnetization from the data below T_c (Fig. 1h) and the DC magnetic susceptibility χ from the data above T_c (red circles, Fig. 1f). The remanent magnetization decreases when temperature T approaches T_c from below; and χ increases dramatically when T approaches T_c from above. In contrast, a thin bulk $CrBr_3$ flake (~10 nm thick) shows a much weaker temperature dependence in susceptibility above T_c and no remanent magnetization below T_c (black squares, Fig. 1f). The lack of remanent magnetization is presumably due to domains or antiferromagnetic ordering from the interlayer exchange and/or dipole-dipole interaction[7,8]. We determine T_c by fitting the temperature-dependent susceptibility to a critical scaling law $\chi \sim (T-T_c)^{-\gamma}$ (Fig. 1g). We obtain $T_c \approx 22.3$ K and 28 K, and critical exponent $\gamma \approx 2.4$ and 1.2 for the monolayer and thin bulk samples, respectively. The value of T_c for the monolayer determined from susceptibility is consistent with the temperature dependence of the magnetization amplitude, which shows a sharp drop near 22.3 K (Fig. 1h). The critical exponent γ of the thin bulk matches well with previous results for bulk $CrBr_3$, and is close to the mean-field value ($\gamma = 1$)[24]. On the other hand, the critical exponent for monolayer $CrBr_3$ is between the predictions of a 2D Ising (γ

= 1.75) and 2D Heisenberg ($\gamma = 3$) model[25,26]. This can potentially be understood from a recent theoretical proposal that 2D $CrBr_3$ is described by a 2D XXZ model with anisotropic exchange interaction[17], and shows a crossover behavior between the Ising and Heisenberg model. Although the exact model to describe 2D $CrBr_3$ is still under debate[17-19], our observation demonstrates its distinct behavior from that of the bulk, and substantial deviation from the mean-field description due to enhanced fluctuations in 2D.

As temperature further approaches T_c (22.3K) from below, the magnetization in monolayer $CrBr_3$ starts to fluctuate spontaneously under zero external magnetic field. Such fluctuations are not observed in the bulk sample under the same experimental conditions (see supplementary movie 1). We analyze both the temporal and spatial dependences of the magnetic fluctuations in monolayer $CrBr_3$. Figure 2a summarizes the fluctuation amplitude map of the magnetization, $\delta M(\boldsymbol{r}) = \sqrt{\langle M(\boldsymbol{r},t)^2\rangle - \langle M(\boldsymbol{r},t)\rangle^2}$, at representative temperatures (see supplementary movie 2-13 for the real-time magnetization fluctuations). Here $M(\boldsymbol{r},t)$ is the out-of-plane magnetization at a given point $(\boldsymbol{r},t)$ in space and time, and the time average $\langle\cdots\rangle$ is equivalent to the ensemble average by assuming ergodicity (see Methods). The magnetization fluctuations first emerge at the corners of the monolayer flake at 21.6 K, quickly expand into the center with increasing temperature, remain large until T_c, then rapidly diminish above T_c. Figure 2c shows the magnetization dynamics at a fixed location P1 (green circle in Fig. 2a) for varying temperatures. The measured magnetization fluctuation dynamics and their temperature dependence resemble the result of a Monte Carlo simulation for a 2D Ising model[27]. Particularly, in the vicinity of T_c, the magnetization shows random values between that of the fully spin-up state (referred to as state "1") and the fully spin-down state (state "0"). This strongly supports that the observed magnetization fluctuations are critical fluctuations. We have also carried out several control

experiments to exclude potential experimental artifacts for the observed magnetization fluctuations (see Supplementary Note 8). Particularly, we have verified that the probe light has no effect on the fluctuations except for a systematic temperature shift of ~ 0.05K.

The central quantity that describes the critical fluctuations is the fluctuation correlation function between magnetizations at point $\boldsymbol{r}_1$ and $\boldsymbol{r}_2$ separated by time Δt (Ref.[1])

$$C(\boldsymbol{r}_1, \boldsymbol{r}_2, \Delta t) = \langle M(\boldsymbol{r}_1, t) M(\boldsymbol{r}_2, t + \Delta t) \rangle - \langle M(\boldsymbol{r}_1, t) \rangle \langle M(\boldsymbol{r}_2, t + \Delta t) \rangle. \quad (1)$$

The temporal correlation at a given point, $C(\boldsymbol{r}_1 = \boldsymbol{r}_2, \Delta t)$, contains direct information of the dynamics in the critical regime. Figure 2d shows the temporal correlation function at position P1 at varying temperatures. It is well described by $e^{-\Delta t/\tau}$, where τ is the correlation decay time. The fluctuations are substantially slowed down at 21.8 K (green curve in Fig. 2c), leading to a marked increase in τ. Figure 2e summarizes the correlation decay time as a function of temperature. The significant slowing-down (up to a second) is a consequence of the enhanced critical magnetic fluctuations in 2D and has been independently confirmed by AC susceptibility measurements (see Methods and Supplementary Note 7 for more discussions). The peak of the correlation decay time, however, occurs at about 0.5 K below the average T_c of the sample (vertical dashed line). A more complete picture is obtained by examining the spatial dependence of the correlation decay time (Fig. 2b). The correlation decay time shows orders-of-magnitude change across the sample at a fixed temperature. It is peaked at slightly different temperatures for different locations. The slowing-down dynamics is in accord with the large fluctuation amplitude shown in Fig. 2a, both occurring within a narrow temperature range (±0.5 K) of T_c and both showing strong spatial inhomogeneity. Potential sources for inhomogeneity include the physical boundary, spatial variations in the carrier doping density (which changes T_c as shown in Fig. 4),

local strain, etc. The extreme sensitivity of magnetic fluctuations to perturbations in the vicinity of the critical point further supports their critical nature.

The critical behavior of the magnetic fluctuations and the spatial inhomogeneity effects are also clearly seen in the spatial correlation function $C(\boldsymbol{r}_1, \boldsymbol{r}_2, \Delta t = 0)$. Figure 3a shows $C(\boldsymbol{r}_1, \boldsymbol{r}_2)$ at several representative temperatures (see Supplementary Note 4 for more temperatures), where $\boldsymbol{r}_1$ is mapped over the entire field of view and $\boldsymbol{r}_2$ is fixed at position P1 (left panel) or P2 (right panel). Below T_c, the correlation functions at both positions are anisotropic with different patterns. The three-fold pattern (P1) and two-fold pattern (P2) at 22.2 K reflect the local geometry of the boundary. Above T_c, on the other hand, the patterns become largely isotropic since the inhomogeneity effect is less important when the long-range magnetic order is destroyed. Figure 3b and 3c show a line cut of the correlation function map for position P1 and P2, respectively, along the dotted lines in Fig. 3a at varying temperatures. The correlation functions feature both an oscillatory component and an exponential envelope function, and can be well fitted by $\cos(\frac{\pi l}{\lambda})\, e^{-\frac{l}{\xi}}$ (solid lines in Fig. 3b and 3c). Here l is the distance to position P1 or P2; and λ and ξ represent the oscillation half-period and the decay length, respectively. An enhanced correlation decay length ξ is seen for both positions near T_c, but it peaks at slightly different temperatures (Fig. 3e), again showing the effect of sample inhomogeneity. The oscillatory component in the spatial correlation is not well understood. It suggests the presence of a domain-like structure with a characteristic width λ (Fig. 3d). The extracted width λ is larger than the sample size for T below ~ 21 K (see Supplementary Movie 2) and decreases rapidly when T approaches T_c. Such a behavior is consistent with the prediction that in 2D ferromagnets even a tiny dipole-dipole interaction becomes increasingly important near T_c and leads to a decreased domain size[28,29].

The sharp temperature dependence of the critical magnetization fluctuations in 2D magnets demonstrated above is fundamentally different from the behavior of non-critical Brownian fluctuations in miniscule systems[30] and opens up opportunities for their efficient control. We fabricate field-effect devices of monolayer $CrBr_3$ with a graphene gate and contact, and achieve tuning of T_c at a rate of ~ -0.4 K/V by applying a gate voltage V_g. Gating primarily introduces doping and tunes the intralayer magnetic exchange coupling in monolayer $CrBr_3$ (See Methods and Supplementary Note 6)[13]. Because critical fluctuations depend sensitively on how close the system is from the critical point, they can be effectively controlled by V_g for instance at a fixed sample temperature. Figure 4a shows the magnetization dynamics of device S2 under different gate voltages at 17.90 K (below T_c at V_g=0 V). The corresponding gate-dependent fluctuation amplitude and the correlation decay time are shown in Fig. 4b. At this temperature, application of $V_g < 0.5$ V can turn on the critical fluctuations that are absent without V_g. In Fig. 4c we demonstrate switching of a magnetic bit by harnessing the critical fluctuations. In the unshaded regions (V_g=0 V), the critical fluctuations are absent, and the magnetic bit stays either in state "1" or state "0" as prepared. In the yellow shaded regions (V_g=0.4 V), the fluctuations are activated. Using real-time feedback control (i.e. removing V_g at the right moment according to the real-time magnetization measurement), one can set the bit into a desired state (see Supplementary Note 5 for similar switching operation in sample S1 with optical control). Because the spontaneous and stochastic fluctuations are the only driving force here, the outcome cannot be deterministic without feedback. For example, Fig. 4d shows that the magnet can be stochastically switched between state "1" and "0" by applying square gate voltage pulses with an amplitude 0.4 V and a pulse width 50 ms (see Methods). Deterministic logical operations can, however, be achieved by making one measurement after each gate pulse and stop the procedure until the desired state is

reached; and in principle the only energy cost of the switching operation is in measuring the system's state. This critical-fluctuation-based concept can therefore potentially provide a solution to efficient magnetic processing and storage, such as logic gates and race-track memory.

We note that complete understanding of the critical fluctuations in 2D $CrBr_3$ will require a sophisticated model that at least accounts for finite magnetic anisotropy, dipolar interaction and the boundary effect in a framework beyond the mean-field theory. It would be interesting to see the potential crossover between different universality classes or the emergence of hidden phases near the critical point[28,29] and real-time imaging of fluctuations can provide invaluable information to that purpose. Nevertheless, our observation clearly demonstrates an unexplored and unique aspect of 2D layered ferromagnets compared to their bulk counterparts. Combining the opportunity to access the critical fluctuation regime in 2D, the device-compatibility of layered materials to enable electrical readout and manipulation, and the magneto-optical imaging technique to monitor magnetization fluctuations in real-time, 2D layered magnets provide an attractive platform for studying spin fluctuations and critical phenomena, as well as for fluctuation-based apparatuses such as dissipationless memories, Brownian motors and reservoir computation.

References

1 Kardar, M. *Statistical Physics of Fields*. (Cambridge University Press, 2007).

2 Gibertini, M., Koperski, M., Morpurgo, A. F. & Novoselov, K. S. Magnetic 2D materials and heterostructures. *Nat Nanotechnol* **14**, 408-419, (2019).

3 Burch, K. S., Mandrus, D. & Park, J. G. Magnetism in two-dimensional van der Waals materials. *Nature* **563**, 47-52, (2018).

4 Dunlavy, M. J. & Venus, D. Critical slowing down in the two-dimensional Ising model measured using ferromagnetic ultrathin films. *Phys Rev B* **71**, 144406, (2005).

5 Djurberg, C. *et al.* Dynamics of an interacting particle system: Evidence of critical slowing down. *Phys Rev Lett* **79**, 5154-5157, (1997).

6 Collins, M. F. *Magnetic Critical Scattering*. (Oxford University Press, 1989).

7 Huang, B. *et al.* Layer-dependent ferromagnetism in a van der Waals crystal down to the monolayer limit. *Nature* **546**, 270-+, (2017).

8 Gong, C. *et al.* Discovery of intrinsic ferromagnetism in two-dimensional van der Waals crystals. *Nature* **546**, 265-+, (2017).

9 Song, T. C. *et al.* Giant tunneling magnetoresistance in spin-filter van der Waals heterostructures. *Science* **360**, 1214-+, (2018).

10 Klein, D. R. *et al.* Probing magnetism in 2D van der Waals crystalline insulators via electron tunneling. *Science* **360**, 1218-+, (2018).

11 Deng, Y. J. *et al.* Gate-tunable room-temperature ferromagnetism in two-dimensional Fe3GeTe2. *Nature* **563**, 94-+, (2018).

12 Huang, B. *et al.* Electrical control of 2D magnetism in bilayer CrI3. *Nat Nanotechnol* **13**, 544-+, (2018).

13 Jiang, S. W., Li, L. Z., Wang, Z. F., Mak, K. F. & Shan, J. Controlling magnetism in 2D CrI3 by electrostatic doping. *Nat Nanotechnol* **13**, 549-+, (2018).

14 Gong, C. & Zhang, X. Two-dimensional magnetic crystals and emergent heterostructure devices. *Science* **363**, 706-+, (2019).

15 Chen, L. B. *et al.* Topological Spin Excitations in Honeycomb Ferromagnet CrI3. *Phys Rev X* **8**, 041028, (2018).

16 Sivadas, N., Okamoto, S., Xu, X. D., Fennie, C. J. & Xiao, D. Stacking-Dependent Magnetism in Bilayer CrI3. *Nano Lett* **18**, 7658-7664, (2018).

17 Lado, J. L. & Fernandez-Rossier, J. On the origin of magnetic anisotropy in two dimensional CrI3. *2d Mater* **4**, 035002, (2017).

18 Xu, C. S., Feng, J. S., Xiang, H. J. & Bellaiche, L. Interplay between Kitaev interaction and single ion anisotropy in ferromagnetic CrI3 and CrGeTe3 monolayers. *Npj Comput Mater* **4**, 57, (2018).

19 Lee, I. *et al.* Fundamental Spin Interactions Underlying the Magnetic Anisotropy in the Kitaev Ferromagnet CrI3. *Phys Rev Lett* **124**, 017201, (2020).

20 Alsnielsen, J. & Birgeneau, R. J. Mean Field-Theory, Ginzburg Criterion, and Marginal Dimensionality of Phase-Transitions. *Am J Phys* **45**, 554-560, (1977).

21 Mermin, N. D. & Wagner, H. Absence of Ferromagnetism or Antiferromagnetism in One- or 2-Dimensional Isotropic Heisenberg Models. *Phys Rev Lett* **17**, 1133-&, (1966).

22 Robinson, P. C. & Bradbury, S. *Qualitative Polarized-Light Microscopy*. (Oxford University Press, 1992).

23 Liu, K. H. *et al.* High-throughput optical imaging and spectroscopy of individual carbon nanotubes in devices. *Nat Nanotechnol* **8**, 917-922, (2013).

24 Ho, J. T. & Litster, J. D. Divergences of Magnetic Properties of Crbr3 near Critical Point. *J Appl Phys* **40**, 1270-&, (1969).

25 Fisher, M. E. Renormalization Group in Theory of Critical Behavior. *Rev Mod Phys* **46**, 597-616, (1974).
26 Wilson, K. G. Renormalization Group - Critical Phenomena and Kondo Problem. *Rev Mod Phys* **47**, 773-840, (1975).
27 Giordano, N. J. *Computational physics*. (Second edition. Upper Saddle River, NJ : Pearson/Prentice Hall, [2006] ©2006, 2006).
28 Kashuba, A. & Pokrovsky, V. L. Stripe Domain-Structures in a Thin Ferromagnetic Film. *Phys Rev Lett* **70**, 3155-3158, (1993).
29 Portmann, O., Vaterlaus, A. & Pescia, D. An inverse transition of magnetic domain patterns in ultrathin films. *Nature* **422**, 701-704, (2003).
30 Jia, D. D., Hamilton, J., Zaman, L. M. & Goonewardene, A. The time, size, viscosity, and temperature dependence of the Brownian motion of polystyrene microspheres. *Am J Phys* **75**, 111-115, (2007).

Methods:

Sample preparation: Thin flakes of $CrBr_3$ encapsulated by hexagonal boron nitride (hBN) on both sides were employed in this study. The hBN-$CrBr_3$-hBN stacks were fabricated using a dry transfer method[31]. $CrBr_3$ and hBN flakes were first exfoliated from their bulk crystals onto silicon substrates with a 300-nm oxide layer. The thickness of hBN and thicker flakes of $CrBr_3$ was determined by atomic force microscopy. The thickness of 2D $CrBr_3$ was determined from the calibrated optical reflection contrast (see Supplementary Note 1). A stamp made of polycarbonate (PC) on polydimethylsiloxane (PDMS) was used to pick up the top hBN flake, the $CrBr_3$ flake and the bottom hBN flake from Si substrates in sequence at 40°C. For gate-tunable monolayer $CrBr_3$ device S2, two additional bilayer graphene flakes were exfoliated from bulk crystals and picked up during the assembly, serving as the contact and back gate, respectively. The complete structure was then stamped onto a clean silicon substrate with pre-patterned gold electrodes at 120°C to delaminate the PC film with the heterostructure from the PDMS layer. The residual PC was dissolved in chloroform at room temperature. The transfer process was performed inside a nitrogen gas filled glovebox with less than 1 part per million (ppm) oxygen and moisture to avoid degradation of the $CrBr_3$ flakes.

Real-time MCD imaging: A 409-nm laser diode (Thorlabs L405P150) was used as the probe light source. The photon energy was chosen to be slightly below the absorption edge of $CrBr_3$ to enhance the magneto-optical sensitivity. Two Glan-Taylor polarizers (Thorlabs GT10), one broadband half-wave plate (Thorlabs AHWP05M-600) and one broadband quarter-wave plate (Thorlabs AQWP05M-600) were used to control and analyze the polarization of the probe beam. The probe beam transmitted through a beamsplitter (Thorlabs BS028) and an objective (Olympus LUCPlanFLN 40x, NA = 0.6), and impinged on the sample. The beamsplitter was mounted on a

post by epoxy to minimize strain and polarization distortion from strain. Samples were mounted in a Montana cryostation (Standard series). An out-of-plane magnetic field was applied through a home-made coil surrounding the sample chamber with a maximum field strength of 20 Oe. The incident intensity of the probe beam on the sample was 0.09 $\mu W/\mu m^2$ for all the measurements presented in the text. For control experiment with different probe beam intensities, see Supplementary Note 8. A 2D electron-multiplying CCD camera (Princeton Instruments, ProEM 512x512) was used to detect reflected light for real-time imaging.

Measurement of magnetic properties away from T_c: The hysteresis loop of $CrBr_3$ monolayer (Fig. 1e) and the DC magnetic susceptibility of both the $CrBr_3$ monolayer and the thin bulk $CrBr_3$ (Fig. 1f and 1g) were obtained from the magnetization-magnetic field (M-H) dependence under an external magnetic field provided by the home-made coil. The magnetization of each flake was obtained by averaging the magneto-optical contrast over a 3×3 μm region in the center of the flake. For temperatures close to T_c, the M-H curve of monolayer $CrBr_3$ becomes ill-defined due to the stochastic critical spin fluctuations at the macroscopic scale. Remanent magnetization in Fig. 1h is obtained by averaging the magneto-optical contrast over the 3×3 μm region and 70 second to average out fluctuations.

Extraction of the correlation functions from real-time images: The temporal and spatial correlation functions (Fig. 2 and 3) were obtained directly from the real-time images of the magnetization fluctuations following the definition given in the text. The average was calculated as a time average over 5000 frames (taken at 70 frames per second) at each temperature. We note that, owing to the importance of the spatial inhomogeneity effect, common analysis methods that require spatial averaging, such as the Fourier transform[32], become not applicable. The time average adopted in this study is closer to the original definition of the ensemble average given

the uniformity in time at equilibrium, and can directly provide information on the effects of spatial inhomogeneity.

Unusually strong critical slowing-down in 2D $CrBr_3$: Although critical fluctuations in principle can occur at any timescale, critical dynamics observed in solid-state spin systems is usually faster than a millisecond[4,33]. To further verify the remarkable critical slowing-down in 2D $CrBr_3$ observed in real-time imaging, we performed AC susceptibility measurement as an independent probe. AC susceptibility is commonly used to determine the relaxation time of a system and its critical dynamics[4,5]. Prominent critical slowing-down is observed in monolayer $CrBr_3$ with timescales over a hundred milliseconds, but not in a ~ 10 nm thin bulk reference sample (see Supplementary Note 7). The good agreement between the AC susceptibility and real-time imaging measurements further confirms that the observed fluctuations are from the intrinsic critical behaviors of 2D $CrBr_3$. The differences between the monolayer and bulk $CrBr_3$ samples support enhanced critical fluctuations in 2D.

Magnetic switching of 2D $CrBr_3$: Measurement was performed to determine the state of a magnetic bit following the application of a square gate pulse that temporarily enables critical fluctuations. Gate pulses of variable amplitude and width were generated by a digital delay/pulse generator (Stanford Research DG535), which was triggered by a data acquisition (DAC) card (National instruments USB-6212). In Fig. 4d, the gate pulses have an amplitude 0.4 V and a pulse width 50 ms. The DAC card also triggered the electron-multiplying CCD camera to synchronize the electrical control and the MCD imaging. Measurement of the magnetization of the bit was made 200 ms after the start of each pulse to ensure that V_g and hence critical fluctuations are turned off. The above process was repeated with periodicity of 300 ms to obtain measurement sequences as exemplified in Fig. 4d.

Data availability:

The data that support the findings of this study are available within the paper and its Supplementary Information. Additional data are available from the corresponding authors upon request.

References for Methods

31 Wang, L. *et al.* One-Dimensional Electrical Contact to a Two-Dimensional Material. *Science* **342**, 614-617, (2013).

32 Honerkamp-Smith, A. R., Veatch, S. L. & Keller, S. L. An introduction to critical points for biophysicists; observations of compositional heterogeneity in lipid membranes. *Bba-Biomembranes* **1788**, 53-63, (2009).

33 Zhang, J. *et al.* Discovery of slow magnetic fluctuations and critical slowing down in the pseudogap phase of YBa2Cu3Oy. *Sci Adv* **4**, aao5235, (2018).

Competing interests:

The authors declare no competing interests.

Acknowledgements

We acknowledge discussions with J. Sethna and J. Kent-Dobias. This work was supported by the National Science Foundation (NSF, DMR-1807810) for the development of the magneto-optical imaging microscope, the ARO Award W911NF-17-1-0605 for sample and device fabrication, the Cornell Center for Materials Research with funding from the NSF MRSEC program (DMR-1719875) for optical characterizations, and the Air Force Office of Scientific Research under award number FA9550-19-1-0390 for data analysis. The growth of hBN crystals was supported by the Elemental Strategy Initiative of MEXT, Japan and CREST (JPMJCR15F3). K.F.M. acknowledges support from a David and Lucille Packard Fellowship. C.J. acknowledges support from a Kavli Postdoctoral Fellowship. Z.T. acknowledges support from THE WATT W. WEBB Graduate Fellowship in Nanoscience.

Author contributions

C.J. conceived the experiment. C.J. and Z.T. developed the measurement technique and performed the experiment and analysis; Z.T. prepared the samples and K.K. fabricated the devices. K.W. and T.T. grew the bulk hBN crystals. C.J., K.F.M. and J.S. co-wrote the manuscript. All authors discussed the results and commented on the manuscript.

Figure captions

Figure 1 | Polarization-enhanced magnetic circular dichroism (MCD) imaging of 2D $CrBr_3$. **a**, Illustration of the experimental setup. Blue and red beams represent illumination light from the laser and scattered light from the sample. They have different effective numerical-apertures. HWP: Half-wave plate. QWP: Quarter-wave plate. **b-d**, Optical microscopy image (**b**) and polarization-enhanced MCD image (**c**, **d**) of a monolayer $CrBr_3$ sample S1 (white dashed box). The MCD image shows giant optical contrast of ±60% for the positive (**c**) and negative (**d**) remanent magnetization. Green dashed box indicates another 2D $CrBr_3$ flake nearby. Scale bar is 5 μm. **e**, Optical contrast of the monolayer against magnetic field shows a hysteresis loop at temperatures below T_c (22.3 K) and paramagnetic behavior above T_c. **f**, **g**, Temperature dependence of the DC magnetic susceptibility of the monolayer (red) and a bulk of ~10 nm thickness (black) (**f**), and the corresponding power law fitting as described in the text (**g**). (**h**) Temperature-dependent remanent magnetization amplitude of the monolayer shows a sharp drop near T_c. Results in **e**-**h** are the averaged properties of a 3 x 3 μm area near the center of the sample.

Figure 2 | Real-time imaging of critical fluctuations in 2D $CrBr_3$. a, Temperature-dependent amplitude map of magnetization fluctuations in sample S1. The critical fluctuations emerge first at the corners of the sample and exist in a narrow temperature range of ~ 0.5 K around the critical point (22.3 K). **b**, Map of fluctuation correlation decay time at representative temperatures. **c**, **d**, Magnetization time trace (**c**) and temporal correlation function (**d**) of position P1 (green circle in **a**) at varying temperatures, showing prominent slowing-down around 21.8 K. The temporal correlation functions are normalized to 1 at zero delay. **e**, Temperature dependence of the correlation decay time (symbols) and uncertainty (error bars) from exponential function fitting of the temporal correlation function of **d**. Error in temperature is smaller than the symbol size. Vertical dashed lines represent the average T_c of the sample.

Figure 3 | Spatial correlation function. a, Spatial correlation function for position P1 (left) and P2 (right) at representative temperatures. The correlation patterns are anisotropic and distinct between the two points below T_c, and largely isotropic and similar above T_c. **b**, **c**, Normalized spatial correlation function for P1 (**b**) and P2 (**c**) along the dotted lines in **a**, which are roughly perpendicular to the domain-like structures. Symbols are experiment and solid lines are fits described in the text. Results for different temperatures are displaced vertically and successively by 0.6 for clarity. **d**, **e**, Domain width (**d**) and correlation decay length (**e**) obtained from fitting the spatial correlation function of P1 (black) and P2 (red). Error bars are standard deviations of the fitting parameters. Vertical dashed lines represent the average T_c of the sample. The characteristic domain width shows a monotonic decrease for both positions as temperature approaches T_c from below. The correlation decay length peaks near T_c, but deviates slightly from P1 to P2 indicating spatial inhomogeneity.

Figure 4 | Electrical control of the critical fluctuations. a, Magnetization time traces of position P3 in monolayer $CrBr_3$ device S2 with graphene back gate. The gate voltage V_g dramatically changes the critical fluctuations through tuning T_c. **b**, Gate-dependent amplitude (black) and correlation decay time (red) of critical fluctuations extracted from the time traces in **a**. **c**, At 17.90K (slightly below T_c at V_g =0V), the critical fluctuations are absent without gate voltage (unshaded regions) and the magnetization stays in state "1" or "0" (red dashed lines). A V_g (=0.4V) is used to temporarily turn on the critical fluctuations (yellow shaded regions). A specific state is written into the magnet by removing gate voltage at the right moment according to the real-time magnetization measurements. **d**, Switching between state "1" and "0" by applying square gate voltage pulses with an amplitude 0.4 V and a pulse width 50 ms at 17.90K (see text and Methods for details). A representative sequence of 100 measurements is shown.

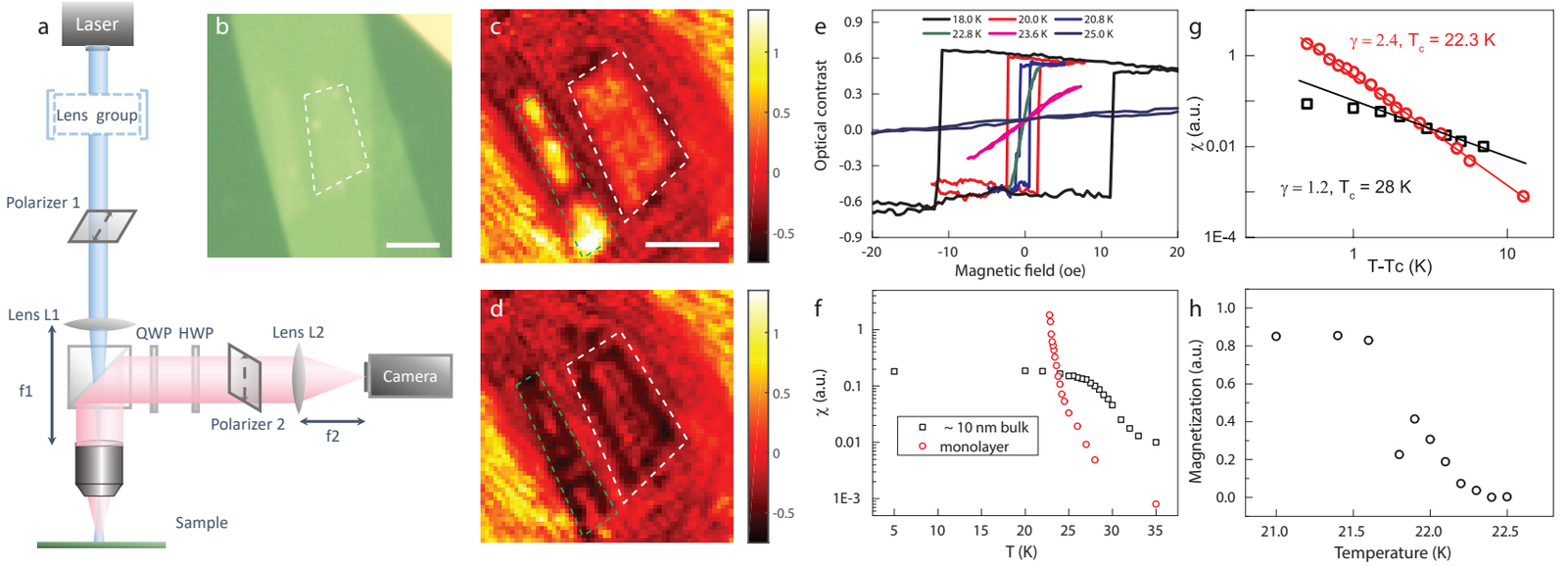
a
Laser
Lens group
Polarizer 1
Lens L1
QWP HWP
Lens L2
Camera
f1
Polarizer 2
f2
Sample
b
c
d
e
18.0 K
20.0 K
20.8 K
22.8 K
23.6 K
25.0 K
Optical contrast
Magnetic field (oe)
f
~ 10 nm bulk
monolayer
χ (a.u.)
T (K)
g
γ = 2.4, T_c = 22.3 K
γ = 1.2, T_c = 28 K
χ (a.u.)
T-Tc (K)
h
Magnetization (a.u.)
Temperature (K)

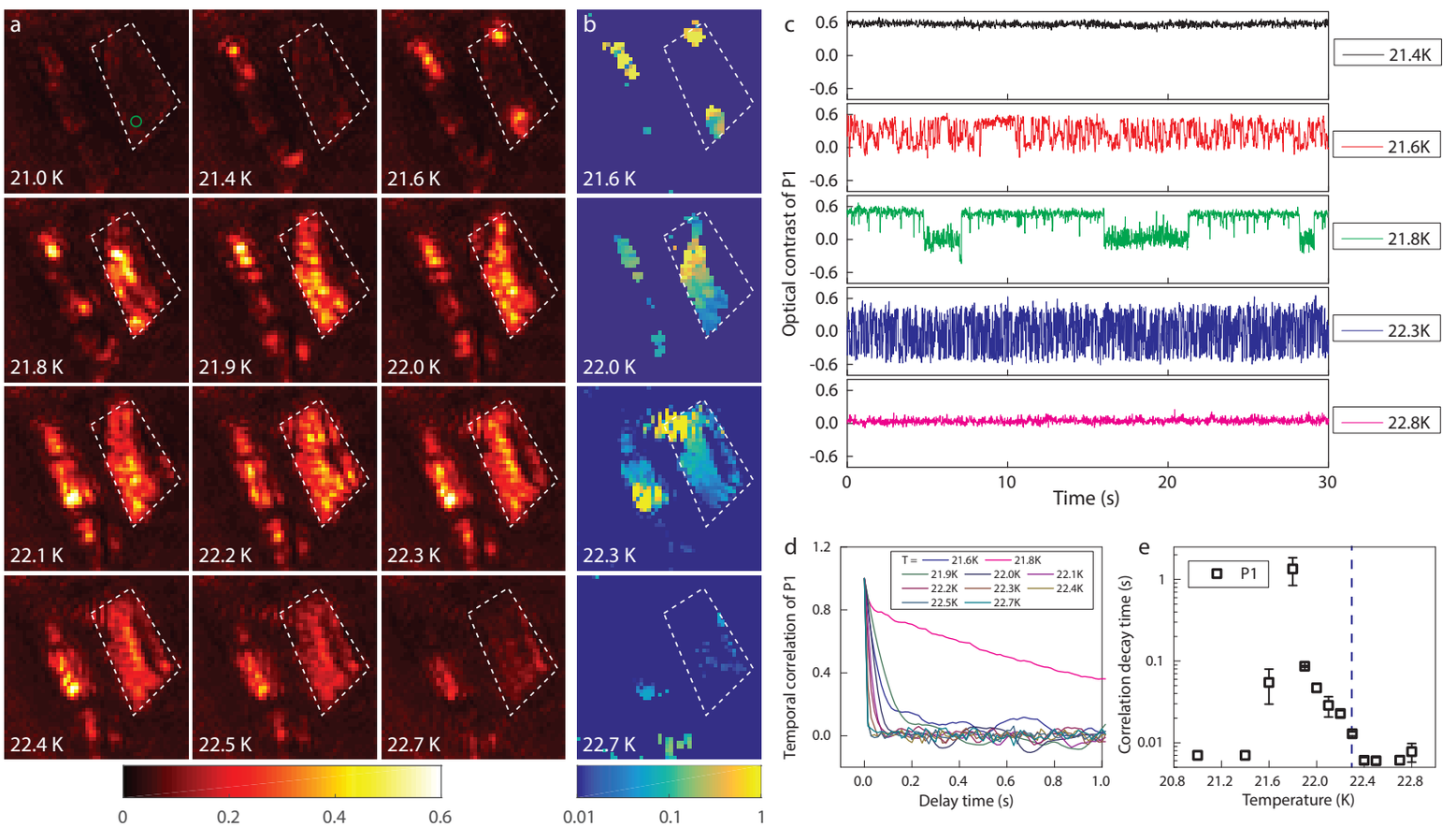
a
21.0 K
21.4 K
21.6 K
21.8 K
21.9 K
22.0 K
22.1 K
22.2 K
22.3 K
22.4 K
22.5 K
22.7 K
0
0.2
0.4
0.6
b
21.6 K
22.0 K
22.3 K
22.7 K
0.01
0.1
1
c
Optical contrast of P1
0.6
0.0
-0.6
21.4K
21.6K
21.8K
22.3K
22.8K
0
10
20
30
Time (s)
d
Temporal correlation of P1
1.2
0.8
0.4
0.0
T =
21.6K
21.8K
21.9K
22.0K
22.1K
22.2K
22.3K
22.4K
22.5K
22.7K
0.0
0.2
0.4
0.6
0.8
1.0
Delay time (s)
e
Correlation decay time (s)
P1
1
0.1
0.01
20.8
21.2
21.6
22.0
22.4
22.8
Temperature (K)

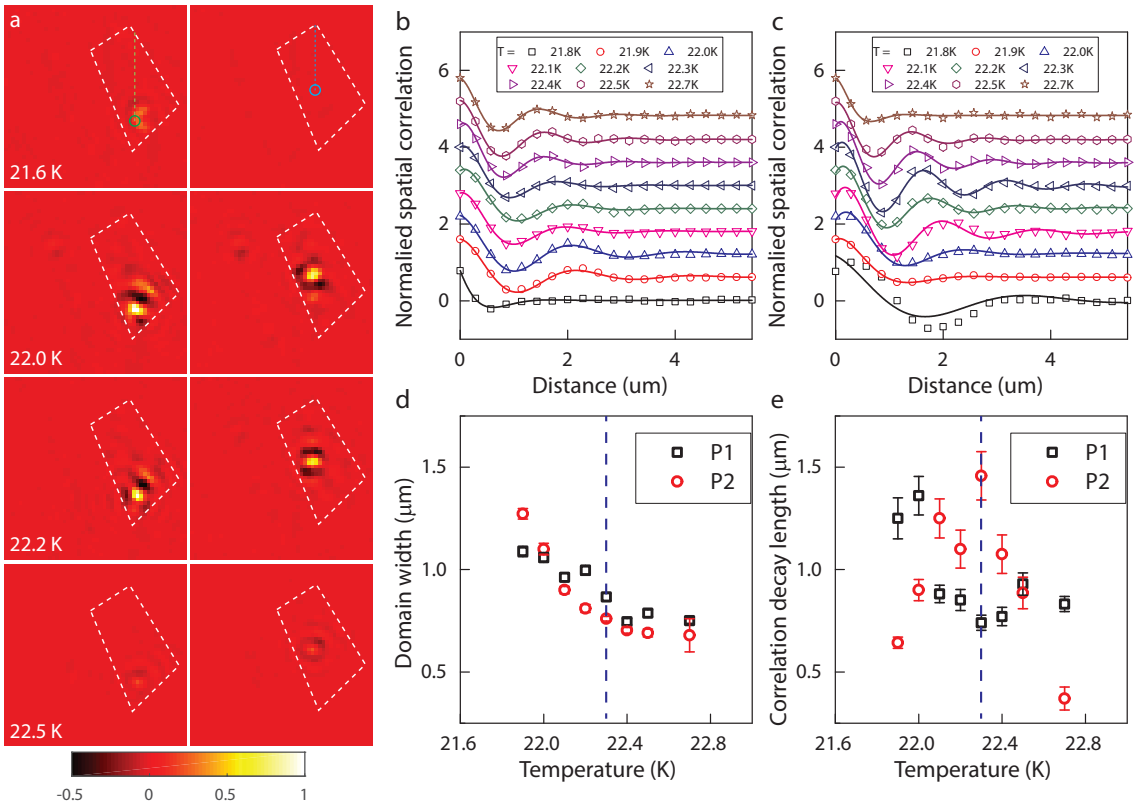
a
21.6 K
22.0 K
22.2 K
22.5 K
-0.5
0
0.5
1
b
Normalied spatial correlation
T = 21.8K 21.9K 22.0K
22.1K 22.2K 22.3K
22.4K 22.5K 22.7K
Distance (um)
c
Normalied spatial correlation
Distance (um)
d
Domain width (μm)
P1
P2
Temperature (K)
e
Correlation decay length (μm)
Temperature (K)

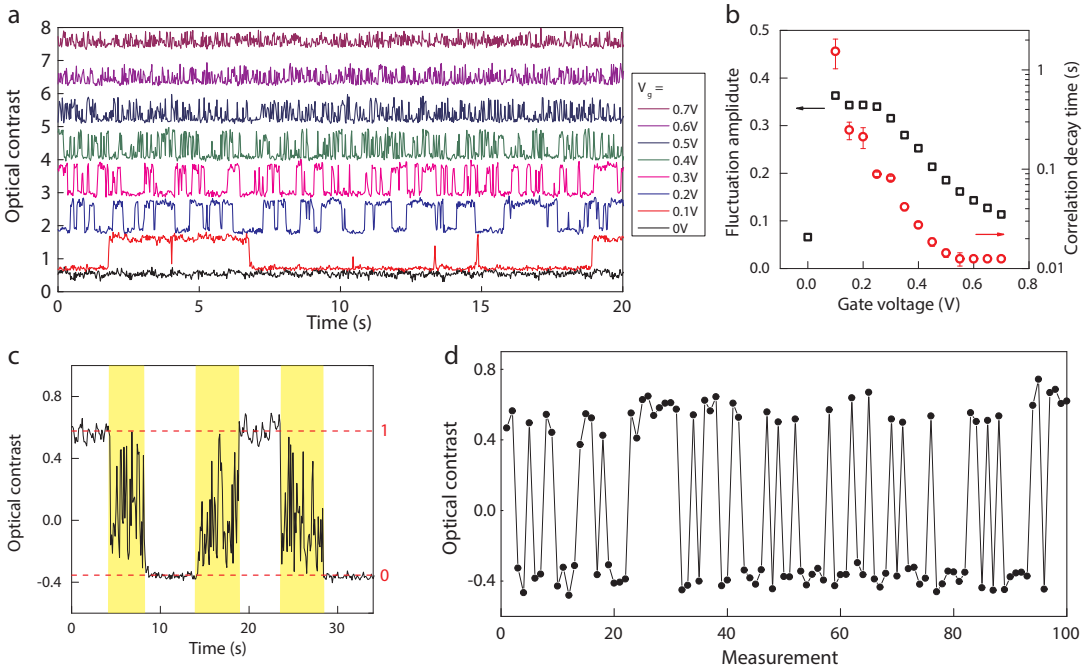
a
Optical contrast
Time (s)
V_g =
0.7V
0.6V
0.5V
0.4V
0.3V
0.2V
0.1V
0V
b
Fluctuation amplidute
Correlation decay time (s)
Gate voltage (V)
c
Optical contrast
Time (s)
1
0
d
Optical contrast
Measurement